

On the Decadal and Multidecadal Variability of the Agulhas Current

RUIZE ZHANG,^{a,b} SHANTONG SUN,^c ZHAOHUI CHEN,^{a,b} HAIYUAN YANG,^{a,b} AND LIXIN WU^{a,b}

^a *Frontier Science Center for Deep Ocean Multispheres and Earth System (FDOMES)/Academy of the Future Ocean and Physical Oceanography Laboratory, Ocean University of China, Qingdao, China*

^b *Laoshan Laboratory, Qingdao, China*

^c *Department of Earth, Ocean and Atmospheric Science, Florida State University, Tallahassee, Florida*

(Manuscript received 7 June 2022, in final form 14 December 2022)

ABSTRACT: The Agulhas Current (AC) is a critical component of global ocean circulation. However, due to a lack of multidecadal observations, it is not clear how the AC has changed in response to anthropogenic forcing. A recent observational study suggests a broadening and slight weakening of the AC in the past few decades, while others suggest a strengthening of the AC during the historical period. In this paper, we find substantial internal variability of the AC on decadal to multidecadal time scales in high-resolution models. We show that the AC consistently exhibits two modes of decadal and multidecadal (i.e., low frequency) variability in a series of high-resolution climate models: a uniform mode that is largely associated with changes in the AC strength and a dipole mode that is mainly related to width changes of the AC. We demonstrate that the uniform mode is mainly forced externally by the decadal variations of the wind field and presents a decline under global warming, suggesting a weakening of the AC in response to anthropogenic forcing. The dipole mode, on the other hand, is mainly due to internal dynamics and does not show a trend during the historical period. Using a quasigeostrophic model that captures the dipole mode, we attribute the dipole mode to low-frequency potential vorticity changes in the western boundary, driven by a divergence of relative potential vorticity due to eddy activity. Thus, our results present further context for the interpretation of the AC responses in a changing climate based on a short observational record.

KEYWORDS: Indian Ocean; Ocean circulation; Climate change; Decadal variability

1. Introduction

The Agulhas Current (AC) system in the southwest Indian Ocean is a critical component of the climate system (Beal et al. 2011). Originating from the Mozambique Channel and the Southeast Madagascar Current, the AC flows southwestward along the east coast of Africa, transporting around 76 Sv (1 Sv = $10^6 \text{ m}^3 \text{ s}^{-1}$) of warm water poleward (Beal et al. 2015; McMonigal et al. 2022). After passing the southern tip of Africa, the AC retroflects back into the Indian Ocean and flows toward the east as the Agulhas Return Current. At the retroflection, the AC leaks warm and salty waters into the Atlantic Ocean as eddies and surface filaments (Biaostoch et al. 2008a; Rühls et al. 2013; Wang et al. 2016), i.e., the Agulhas leakage. The Agulhas leakage connects the Indian Ocean and the Atlantic Ocean, acts as a crucial returning pathway of the global ocean overturning circulation (Weijer et al. 2001; Talley 2013), and could potentially modulate the variability of the Atlantic meridional overturning circulation (Biaostoch et al. 2008b).

Both the AC transport and pathway exhibit variability on a range of time scales. Based on 3 years of in situ mooring observations and two decades of sea surface height data, Beal et al. (2015) found substantial seasonal variations of the AC transport, which peaks in the austral summer. On interannual time scales, observations and reanalysis data suggest that the AC transport is largely constrained by the overlying atmospheric circulation, which is modulated by El Niño–Southern Oscillation (ENSO) and the Southern Annular Mode (SAM) (Elipot and Beal 2018). The AC pathway is occasionally interrupted by solitary cyclonic meanders on intra-annual time scales near the coast of Port Elizabeth (34°S, 25°E), the Natal pulse (Krug and Penven 2011), associated with high-frequency sea surface temperature variability. Tsugawa and Hasumi (2010) analyzed the generation mechanisms of the Natal pulse using a high-resolution regional ocean model. They concluded that anticyclonic eddies from the upstream AC is responsible for triggering the Natal pulse through barotropic instability, which is later confirmed by Elipot and Beal (2015) using in situ observations. The Natal pulse also shows interannual variations, which have been linked to large-scale wind variability in the southern Indian Ocean (Yamagami et al. 2019).

In this study, we focus on the low-frequency variability of the AC system on decadal to multidecadal time scales. The long-term changes of AC have been examined in a number of studies over the past two decades, using both observations (Rouault et al. 2009; McMonigal et al. 2022; Gunn et al. 2022) and numerical models (Cai 2006; Sen Gupta et al. 2021). However, it remains debatable whether the AC transport has changed significantly during the historical period in response

Denotes content that is immediately available upon publication as open access.

Supplemental information related to this paper is available at the Journals Online website: <https://doi.org/10.1175/JPO-D-22-0123.s1>.

Corresponding author: Zhaohui Chen, chenzhaohui@ouc.edu.cn

DOI: 10.1175/JPO-D-22-0123.1

© 2023 American Meteorological Society. For information regarding reuse of this content and general copyright information, consult the [AMS Copyright Policy](#) (www.ametsoc.org/PUBSReuseLicenses).

to greenhouse gas forcing and previous studies have reached contradictory conclusions. Using a high-resolution (0.1°) regional model nested to a relatively coarse-resolution (0.5°) global ocean model, forced by reanalysis atmospheric boundary conditions, [Biastoch et al. \(2009\)](#) suggests that the AC transport, at 32°S , decreased by around 5 Sv from 1970 to 2004. However, using a Regional Oceanic Modeling System (ROMS) with a 0.25° resolution, [Rouault et al. \(2009\)](#) suggests a strengthening of the AC from 1982 to 2001. More recently, building on both in situ observations and sea surface height data, [Beal and Elipot \(2016\)](#) suggested that the AC is broadening, with only a slight decrease of 1 Sv since the early 1990s. The broadening was attributed to an increase in eddy activity in the AC region. However, it is not clear whether this broadening is a forced response to a changing climate or due to intrinsic dynamics.

The discrepancy in long-term changes of the AC between different studies could be due to either the insufficient length of observations or the different representation of eddies, which are key to the AC variability. The long-term change in AC may be aliased with its variations on decadal and multidecadal time scales, which could stem from either oceanic intrinsic variability or external atmospheric forcing. Thus, to better understand the responses of the AC system in a warming climate, it is crucial to separate the long-term trend from its low-frequency variability and to uncover the underlying mechanisms that determine the long-term change of AC on different time scales. To achieve this goal, we use a state-of-the-art high-resolution model Community Earth System Model (CESM) and a group of HighResMIP models in phase 6 of the Climate Model Intercomparison Project (CMIP6) to examine the decadal and multidecadal variability of the AC and its response to global warming.

The paper is organized as follows. [Section 2](#) gives a brief description of the model simulations used in this study. In [section 3](#), we quantify the low-frequency variability of AC and its response to global warming in CESM and the HighResMIP simulations. The mechanisms that account for the low-frequency variability of AC are explained in [section 4](#) using a quasigeostrophic model, followed by some discussions in [section 5](#). [Section 6](#) summarizes the results.

2. Description of the high-resolution model simulations

a. CESM

The output from a fully coupled high-resolution climate model, released by the International Laboratory for High-Resolution Earth System Prediction (iHESP), is used in this study ([Chang et al. 2020](#)). It was carried out using the NCAR Community Earth System Mode (CESM) version 1.3. The atmosphere and land components of CESM have a nominal horizontal resolution of 0.25° . The ocean component, Parallel Ocean Program version 2 (POP2), has a horizontal resolution of nominal 0.1° and is fine enough to resolve the structure of AC and the eddy-mean flow interactions along the AC ([Hallberg 2013](#)). We focus on two experiments by CESM 1.3: a preindustrial control experiment and a historical experiment. The 500-yr preindustrial control experiment, initialized from the climatological

data of *World Ocean Atlas 2013* in January, is forced under climate conditions that represent 1850. The historical simulation is branched from the preindustrial control experiment at year 250, and it is forced by the historical climate condition from 1850 to 2005. Thus, the differences between the preindustrial control and historical experiments represent a forced response to the increasing greenhouse gas forcing during the historical period. We use monthly-mean output during model years 200–500 in the preindustrial control experiment and 1870–2005 in the historical experiment to show the low-frequency variability of the AC. The daily outputs, which are available only during years 338–450 in the preindustrial control experiment and 1877–2005 in historical experiment, are used in analysis of the dynamic mechanisms. A more detailed description of this high-resolution dataset can be found in [S. Zhang et al. \(2020\)](#).

b. HighResMIP

To investigate whether the results are model dependent, we also use output from the CMIP6 HighResMIP experiments ([Haarsma et al. 2016](#)). The HighResMIP is the first high-resolution coupled climate model intercomparison project, which is designed to systematically investigate the impact of model resolutions on climate simulations ([Roberts et al. 2020](#)). The 11 HighResMIP datasets used in this study include 9 models with an eddy-permitting (horizontal resolution 0.25°) ocean component (HadGEM3-GC31-HM1, HadGEM3-GC31-HM2, HadGEM3-GC31-HM3, HadGEM3-GC31-MM1, HadGEM3-GC31-MM2, HadGEM3-GC31-MM3, CMCC-CM2-HR4, CMCC-CM2-VHR4, CNRM-CM6-1-HR) and 2 models with eddy-resolving (horizontal resolution 0.1°) ocean component (CESM-TAMU, HadGEM3-GC31-HH1). All HighResMIP models used in this study are forced by the same historical forcing (1950–2014) and the high-end emission scenario of the Shared Socioeconomic Pathways (SSPx; 2015–50), in accordance with the CMIP6 experimental protocol.

3. Low-frequency variability of the AC in high-resolution climate models

We investigate the low-frequency variability of the AC in high-resolution climate models and examine the processes that may contribute to the variability. We focus on velocity field perpendicular to a section across the AC from 33.05° to 34.45°S . This section is roughly collocated with the Agulhas Current Time Series Experiment (ACT) array and the Agulhas System Climate Array (ASCA) ([Beal et al. 2015](#); [Gunn et al. 2020](#); [McMonigal et al. 2020](#)). As in observations, the AC is surface intensified, with a core locating roughly 50 km offshore ([Fig. 1b](#); [Beal et al. 2015](#)). The volume transport of the Agulhas Current in the high-resolution CESM simulations show substantial variability. Its time-mean value and standard deviation are about 84 and 22 Sv, specifically. This is comparable to the ACT and ASCA observation, in which the mean and standard deviation are 76 and 22 Sv, respectively. The transport-weighted temperature and transport weighted salinity are also similar to observations ([Fig. S2](#); [Gunn et al. 2020](#); [McMonigal et al. 2020](#)).

We perform an empirical orthogonal function (EOF) analysis on the model-reported velocity field to decompose the

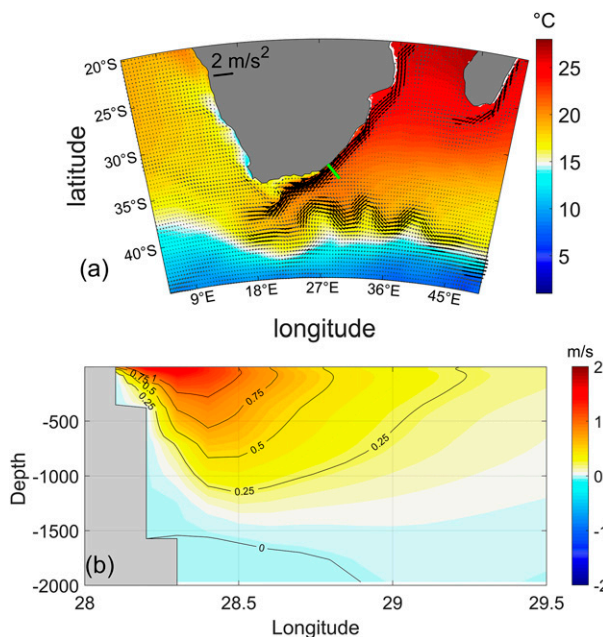


FIG. 1. (a) Mean sea surface temperature (color shading) and surface velocity (black vectors) in the high-resolution CESM historical experiment, averaged over 1850–2005. The green line indicates the cross section of AC we examined in this paper. (b) Current velocity perpendicular to the AC section [green line in (a)] in the upper 2000 m, with positive (negative) values representing southwestward (northeastward) flow.

time–space velocity field of AC and identify the dominant pattern of spatiotemporal structure of the AC (Gunn et al. 2020; McMonigal et al. 2020). Before carrying out the EOF analysis, we perform a 7-yr moving average of the model output to focus on the decadal and multidecadal variability of the AC. A similar approach is taken by Zhang et al. (2010) in examining the low-frequency variability of sea surface temperature. We note that the first 10 years and the last 10 years in preindustrial control and historical experiments have been discarded due to the filtering.

a. Low-frequency variability of the AC and its response to anthropogenic forcing

We identify two predominant modes of the AC variability in the preindustrial control experiment of CESM (Fig. 2), a dipole mode and a uniform mode, which together account for about 90% of the low-pass-filtered AC variance. The dipole mode, which explains about 52% of the variance, is characterized by out-of-phase changes between the core and the flank of AC. The principal component associated with the dipole mode exhibits substantial decadal variability. A positive phase of the dipole mode corresponds to a broadening of the AC in the preindustrial control experiment.

The uniform mode, which accounts for 36% of the AC variance, is characterized by changes of the same sign over the examined section. A closer examination suggests this mode is closely related to changes in the AC volume transport (Fig. 4a).

Like the dipole mode, the uniform mode also exhibits substantial decadal variability. We note that the variability associated with the uniform mode is mostly highlighted at the flank of AC, implying that processes at the flank makes dominant contributions to the low-frequency variability of AC volume transport.

We regress the low-frequency volume transport of the AC to the velocity section examined above (Fig. S3) and find that the regression shows similar structure with the uniform mode. We also choose 25 sections parallel to the AC section mentioned above and perform a similar EOF analysis over the velocity fields averaged from the sea surface to 1000-m depth (Fig. S4). We find that these two modes are robust across these sections (Fig. S5). Additionally, we also tested the impacts of different choices of cutoff window in the moving average, from 5 to 12 years, the results do not appear to be changed substantially. However, when the cutoff window is smaller than 5 years, the results would be dominated by interannual and higher-frequency variability of AC. When the cutoff window is longer than 12 years, the results would be affected because substantial decadal variability of the AC is removed.

The ocean circulation and its variations may also be subject to changes due to anthropogenic forcing (e.g., Yang et al. 2016; Peng et al. 2022). To examine the influence of anthropogenic forcing on the low-frequency variability of the AC, we compare the results above with a historical simulation of CESM, which includes prescribed anthropogenic forcing. Despite the different forcing boundary conditions, the two dominant modes found in the preindustrial control experiment also exist in the historical experiment, except that the two modes switch orders with the uniform mode becoming the leading one (Fig. 3). The two modes explain 86% of the low-pass-filtered AC variance in the historical run. The uniform mode in the historical experiment accounts for over 56% of the total variance, with the dipole mode contributing another 29%. The uniform mode exhibits an upward trend (Fig. 3c), suggesting a decline of the AC during the historical period. This decline of the AC volume transport does not appear to be explained by internal variability of the model and we infer that this is a response to anthropogenic forcing (see discussion in section 5a). The absence of linear trend in the dipole mode suggests that the anthropogenic forcing has limited impact on the width changes of the AC on centennial time scales (cf. Beal and Elipot 2016).

b. Potential dynamics in high-resolution CESM

Here we discuss the physical mechanisms related to the two modes of AC variability in the high-resolution CESM simulations. First, we focus on the uniform mode. The uniform mode is closely correlated with the AC volume transport with a correlation coefficient of 0.86 and 0.92 in the preindustrial control and historical experiments, respectively (Fig. 4). Therefore, we conclude that the uniform mode represents variability in the strength of the Agulhas Current. The AC volume transport is largely determined by the surface wind stress forcing (Sverdrup 1947). By integrating the wind stress curl along 34°S over the Indian Ocean, approximately the same latitude as the AC section, we obtain the AC volume

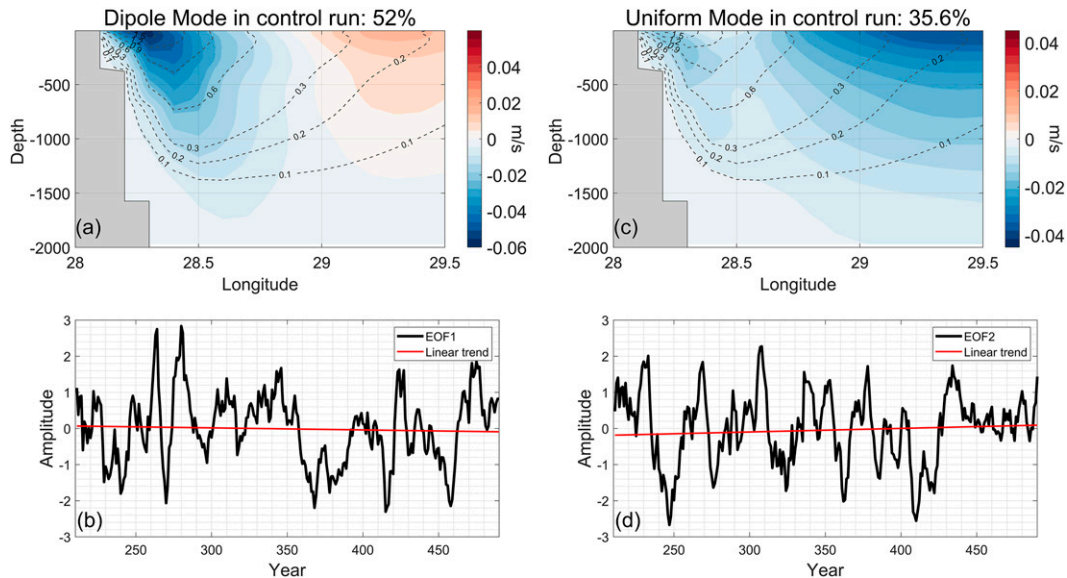


FIG. 2. EOF analysis on the low-pass-filtered (>7 years) current speed across the AC section in the preindustrial control experiment, performed over model years 210–490. (a) Spatial pattern of the dipole mode (shading), overlaid with the mean AC speed across the section (gray dashed contour). (b) Time series of the principal component associated with the dipole mode (black). The red line denotes the linear trend of the principal component. (c) As in (a), but for the uniform mode. (d) As in (b), but for the uniform mode.

transport driven by basin-scale winds (Fig. 4). When the wind stress curl leads 2–5 years, their correlation reaches maximum, with a correlation coefficient of about 0.6. The declining trend of the AC transport in historical experiment is largely explained by the weakening of wind stress forcing in the midlatitude, caused by a poleward shift in the wind field (Yang et al. 2020). The weakening of the Indonesian Throughflow in a warming climate may also contribute to the weakening of the AC transport (Ma et al. 2020).

The dipole mode mainly corresponds to a change in the width of AC. Previously, the multidecadal width changes of the AC have been linked to eddy activity (Beal and Elipot 2016). Here we examine the relationships between the dipole mode and the low-frequency variability of eddy activity. We separate the velocity field into an eddy component and a mean flow component using an 18-month cutoff period (Beal and Elipot 2016). The daily mean output of the velocity field is used to calculate eddy kinetic energy (EKE). The variability

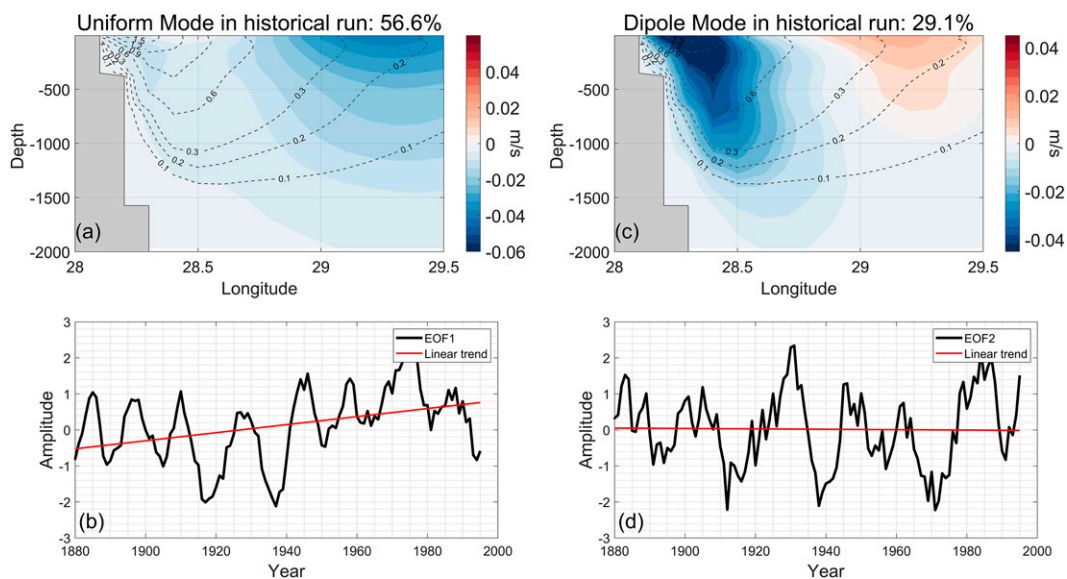


FIG. 3. As in Fig. 2, but for the results from the historical experiment from 1880 to 1995.

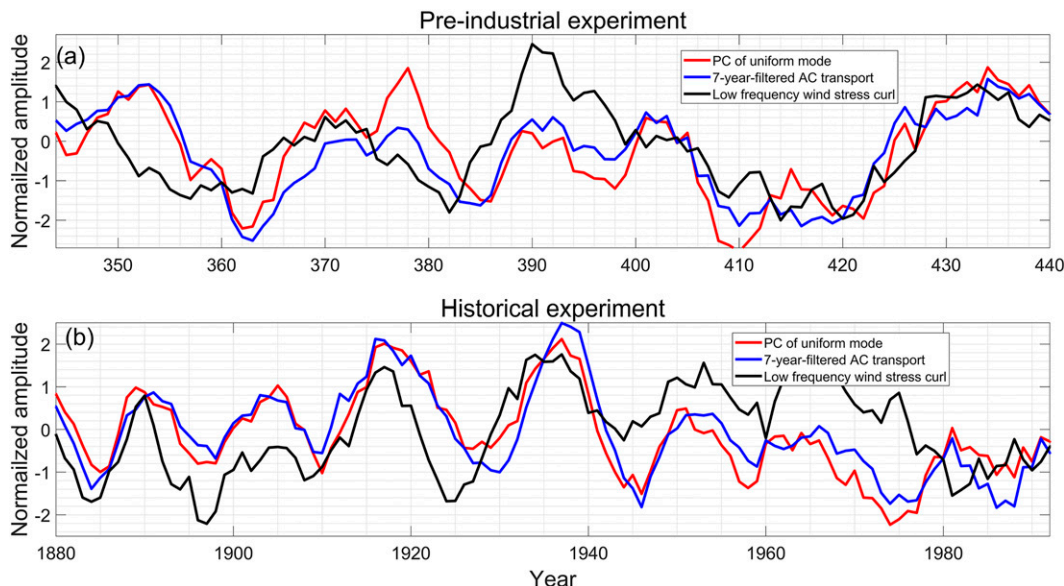


FIG. 4. (a) Comparison of the principal component of the uniform mode (red) with the 7-yr low-pass filtered wind stress curl integrated along 34°S across the Indian Ocean (black) and the low-frequency transport variability of the AC (blue) in the preindustrial control experiment over model years 345–440. (b) As in (a), but for the historical experiment from 1880 to 1995.

of the calculated EKE, thus, excludes changes in the kinetic energy associated with the low-frequency variations (the dipole mode and the uniform mode). We compare the low-frequency variability of EKE with the time series of the dipole mode and find that they are highly correlated with a correlation coefficient of 0.71 and 0.77 in the historical and preindustrial control experiments, respectively (Fig. 5). The high correlation suggests that the dipole mode may be related to the nonlinear interactions between the mean flow and eddies. Therefore, we conclude that the dipole mode is more representative of nonlinear interactions, and we use a two-layer quasigeostrophic model to investigate these dynamical processes further (see section 4).

We also compare the dipole mode with the AC volume transport. Due to the asymmetry of its spatial pattern, the dipole mode is not completely independent of the AC volume transport. Instead, the correlation coefficients between the dipole mode and the AC volume transport are 0.45 and 0.35 in the preindustrial control and historical experiment, respectively, which is much smaller than that in the uniform mode.

c. Results from HighResMIP models

To examine the model dependence of these low-frequency variability, we analyze 11 high-resolution models in HighResMIP. Most of the HighResMIP models (as shown in Figs. S6–S16 in the online supplemental material) show similar results with CESM. All models in HighResMIP exhibit two leading low-frequency variability modes, a uniform mode and a dipole mode. The uniform mode in all models consistently exhibits a trend that is consistent with a weakening AC transport from 1950 to 2050. The trend in the dipole mode is small and the sign of it is inconsistent among different models. Meanwhile, the contribution due to the uniform mode in HighResMIP is larger

than that in the historical and preindustrial control experiment, due to the rapid decline of AC under the high-end emission scenario (Stellema et al. 2019; Sen Gupta et al. 2021). We also compare the relative importance of the dipole model and uniform mode between different models, and examine its dependence on how much the model can resolve eddies (Fig. S17). We find that, as the model resolution increases from 0.25° to 0.1° , the contribution to the AC low-frequency variability due to the dipole mode appears to increase, especially in the HadGEM-GC31 series of model simulations, implying the importance of eddies in the formation of the dipole mode.

4. Low-frequency variability of the AC in a QG model

In the analysis of the CESM model, we highlighted the connections of the dipole model to eddy activity. As the Rossby number and aspect ratio of the Agulhas Current is very small, we could use the quasigeostrophic dynamics to explain the low-frequency variability of AC. In this section, we discuss how eddy activity may have contributed to the low-frequency variability using a two-layer quasigeostrophic (QG) model, which, as we will show below, successfully captures the low-frequency dipole variability of the AC.

a. QG model and experimental design

The quasigeostrophic model is an idealized theoretical model, which has been successfully used to theoretically analyze the low-frequency intrinsic variability of wind-driven circulation and the dynamics of western boundary current (Berloff and McWilliams 1999a; Berloff and Meacham 1998; Berloff et al. 2007; Berloff and McWilliams 1999b; Cessi and Ierley 1995; Yang et al. 2017b). The governing equations for

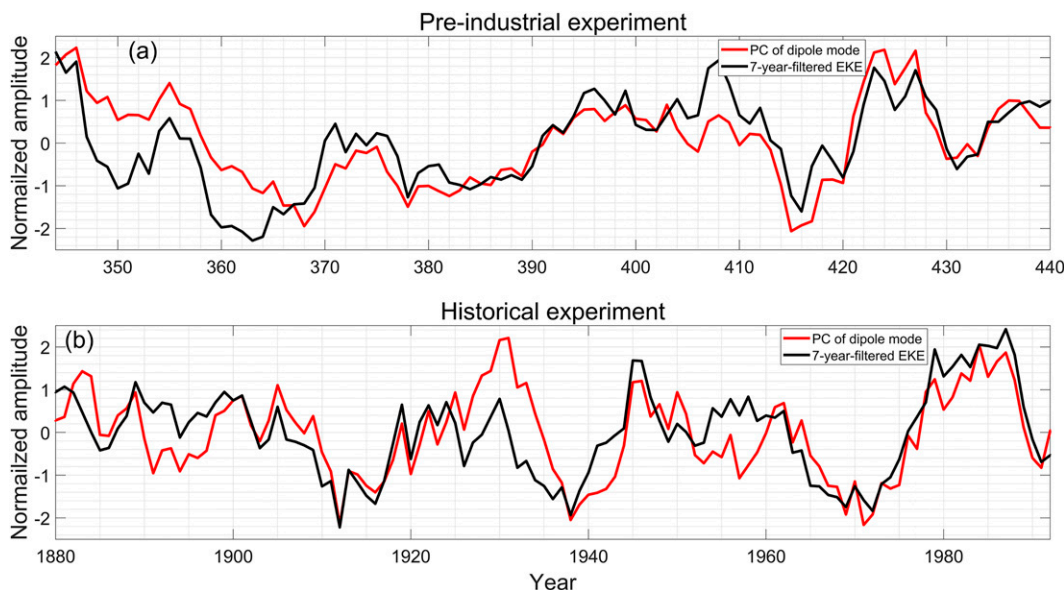


FIG. 5. (a) Comparison of the principal component of the dipole mode (red) with the 7-yr low-pass filtered EKE integrated along the AC section (black) in the preindustrial control experiment over model years 345–440. (b) As in (a), but for the historical experiment over 1880–1995.

the two dynamical isopycnal layers are as follows (Pedlosky 1987; Berloff et al. 2007):

$$\frac{\partial q_1}{\partial t} + J(\psi_1, q_1) = \frac{1}{\rho_0 H_1} \text{curl} \boldsymbol{\tau} + A_H \nabla^4 \psi_1, \quad (1a)$$

$$\frac{\partial q_2}{\partial t} + J(\psi_2, q_2) = A_H \nabla^4 \psi_2 - \gamma \nabla^2 \psi_2. \quad (1b)$$

Here, q_i represents potential vorticity, ψ_i represents streamfunction, and H_i represents the mean thickness of each layer, where the subscripts $i = 1$ and 2 denote the surface and bottom layer, respectively. Lateral friction with a constant dissipation coefficient A_H and bottom friction in Rayleigh form with a constant coefficient γ are both included to dissipate the flow. The Coriolis parameter is approximately as a constant f_0 , and $\boldsymbol{\tau}$ is the wind stress. The potential vorticity for the surface (q_1) and bottom (q_2) layer are defined as follows:

$$q_1 = \nabla^2 \psi_1 + \frac{f_0^2}{g' H_1} (\psi_2 - \psi_1) + \beta y, \quad (2a)$$

$$q_2 = \nabla^2 \psi_2 + \frac{f_0^2}{g' H_2} (\psi_1 - \psi_2) + \beta y. \quad (2b)$$

where g' is the reduced gravity, and β is the meridional gradient in the Coriolis parameter. Under the quasigeostrophic assumption, the potential vorticity is divided into three parts: the relative potential vorticity (RPV) $\nabla^2 \psi_i$, the thickness potential vorticity (TPV) $[f_0^2 / (g' H_i)] (\psi_{3-i} - \psi_i)$, and planetary potential vorticity βy . For more details about the model configuration, readers are referred to Mu et al. (2011) and Sun et al. (2013).

The model domain in this experiment includes the whole south Indian Ocean and part of the South Atlantic Ocean

from 65°S to 0° and from 0° to 115°E. The parameters used in the model are listed in Table 1. The spatial resolution of the QG model is 10 km, which is enough to resolve the AC (120 km wide) and eddies (Smith et al. 2000; Chassignet and Xu 2021; Hallberg 2013), noting that the baroclinic Rossby deformation radius is about 40 km.

To simplify the geometry, the African continent is represented by a combination of a rectangular and a right trapezoid shape, and the island of Madagascar is represented by a rectangular (Fig. 6a). The nonnormal flow and nonslip boundary conditions are used along continental boundaries and domain boundaries. To remove variability externally forced by changes in the wind field, we force the model with a zonal wind stress that is constant in time (Fig. 6b):

$$\tau_x = \tau_0 \cos[2\pi(1.2 - 0.03y/L_y)(y/L_y + 0.12)]. \quad (3)$$

This form of the wind forcing produces a cyclonic gyre circulation to the south of the subtropical gyre, a crude representation of the Southern Ocean. Under the above assumptions, we focus on the midlatitude ocean nonlinear dynamics and the associated ocean intrinsic low-frequency variability. After a spinup

TABLE 1. The reference parameters used in the QG model.

Model parameters			
H_1	1000 m	H_2	3000 m
L_x	11 500 km	L_y	6500 km
ρ_0	1000 kg s ⁻³	g'	0.03 m s ⁻²
f_0	-1.26×10^{-4} s ⁻¹	β	1.75×10^{-11} m ⁻¹ s ⁻¹
A_h	140 m ² s ⁻¹	γ	10 ⁻⁷ m ⁻¹
τ_0	0.23 N m ⁻²		

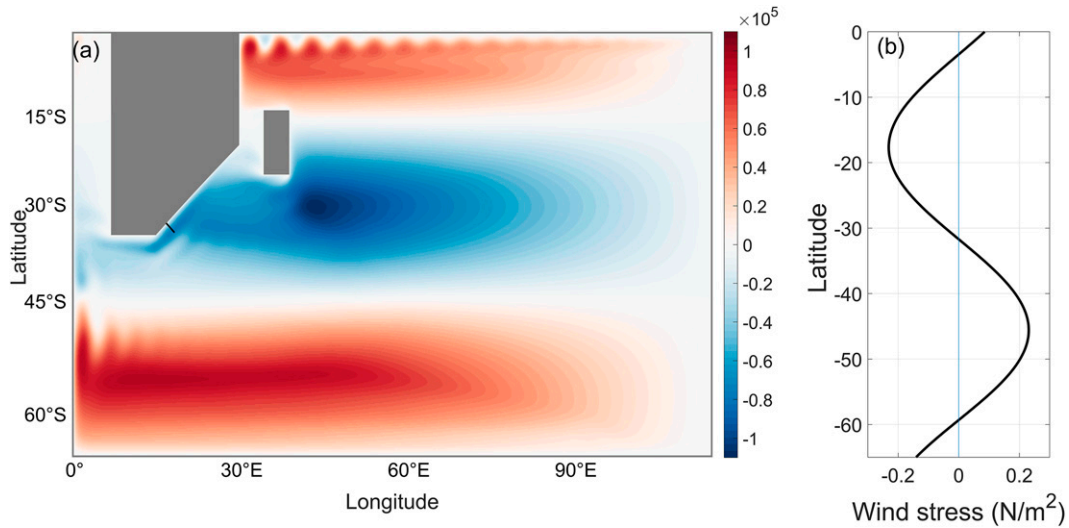


FIG. 6. (a) The domain of the QG model and upper layer streamfunction averaged over model years 1–200. The gray patches represent the lands (African continent and Madagascar island). The black line near the African coast indicates the AC section selected in QG model. (b) Zonal wind stress τ_x , plotted as a function of latitude, which is defined in Eq. (3).

for 200 years from a state of rest, the model is integrated for another 200 years with the output saved every 3 days for analysis.

b. Dipole mode in the QG model

As before, we choose a cross section perpendicular to the coastline of the African continent (black line in Fig. 6a). After a 7-yr low-pass filter, we apply EOF analysis on the upper-layer velocity field along the section to examine the low-frequency variability of the AC. The leading mode (Figs. 7a,c),

which accounts for about 74% of the low-frequency variance, is a dipole mode that resembles the dipole mode in CESM, characterized by out-of-phase changes between the core and the flank of AC. Specifically, in the positive phase of the dipole mode (red in Fig. 7a), the core of AC is approximately 0.1 m s^{-1} stronger than that in the negative phase (blue in Fig. 7a) and the flank of AC shows opposite changes. The dipole mode in the QG simulation has similar spectra with the preindustrial CESM simulation. The presence of the

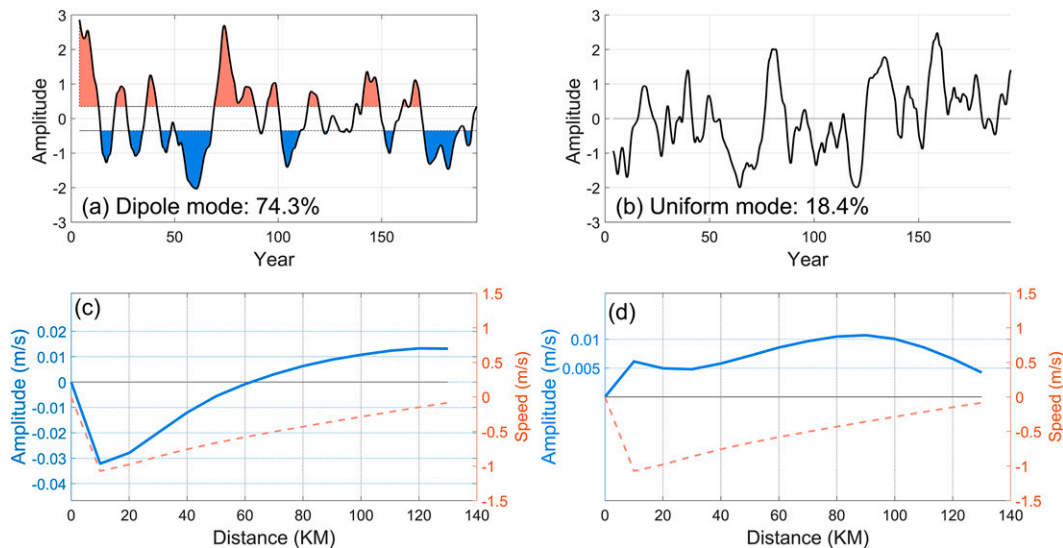


FIG. 7. Results from EOF analysis on the low-pass filtered upper layer velocity along the AC section in the QG model over model years 7–194. (a) Time series associated with the dipole mode in the QG model. Periods with a narrower AC is marked in red and a broader AC is marked in blue. (b) Time series associated with the uniform mode. (c) Spatial pattern of the dipole mode in the QG model (blue solid line). The time-mean AC speed averaged over model years 7–194 across the section is plotted in an orange dotted line for comparison. (d) As in (c), but for the uniform mode.

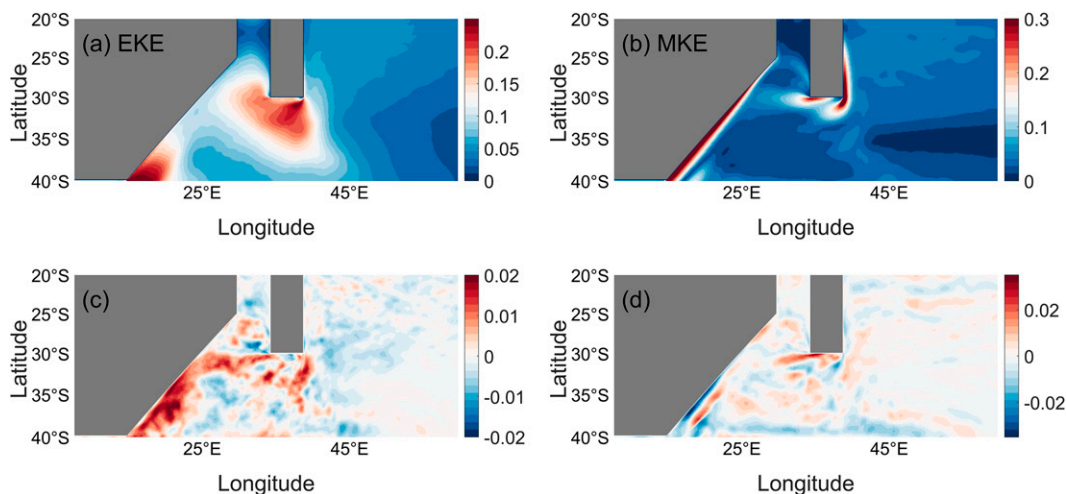


FIG. 8. Distribution of time-mean (a) EKE and (b) MKE in the QG model averaged over model years 7–194. Difference of (c) EKE and (d) MKE between the negative phase (blue in Fig. 8a) and the positive phase of the dipole mode (red in Fig. 7a).

dipole mode, despite an idealized time-independent wind forcing [Eq. (3)], suggests that the dipole mode is likely a result of nonlinear intrinsic processes. A uniform mode is also identified in the QG model, but it plays a much smaller role in the low-frequency variability of the AC and is distinct from the CESM simulation, mainly due to the lack of variability in surface wind forcing (section 3b).

Despite a constant wind forcing, eddy activity exhibits substantial low-frequency variability, highlighting the impact of nonlinear processes in the wind-driven circulation (Chang et al. 2001; Dewar 2003). We now examine the potential role of eddy activity in the dipole mode of the QG model. As in CESM, we separate the flow into a mean component and an eddy component with an 18-month cutoff period. The cutoff period is chosen to be 18-month based on the eddy time scales following previous studies (Berloff et al. 2007; Yang et al. 2015; Beal and Elipot 2016). We then calculate the mean flow kinetic energy (MKE) and the eddy kinetic energy (EKE) (Figs. 8a,b). By making a composite of EKE and MKE during the positive phase (narrower AC; red in Fig. 7a) and the negative phase (wider AC; blue in Fig. 7a) of the dipole mode in QG model, respectively, we show that eddy activity is much stronger during the wider AC period than that during the narrower AC period (Fig. 8c), consistent with CESM (Fig. 5) and observations (Beal and Elipot 2016). Next, we carry out a potential vorticity budget to discuss how eddy activity may help drive the dipole mode.

c. Potential vorticity budget in the QG model

In the QG model, the low-frequency variability of the potential vorticity in the AC region is closely related to the dipole mode (Fig. 9). When the dipole mode is in its positive phase, the AC is narrower with a stronger shear in the mean flow, characterized by a positive potential vorticity anomaly. This relationship also holds in the high-resolution CESM

simulations (Fig. S18). Therefore, we can understand the physical processes that drive the dipole mode by examining the processes that determine the evolution of potential vorticity in the QG simulation. We examine these processes using a budget analysis of potential vorticity, in which we decompose the potential vorticity equation into contributions due to mean flow and eddy activity [Eq. (4)]. Through the budget analysis, we can identify which processes (i.e., mean flow changes, eddy activity changes, lateral dissipation, eddy–mean flow interaction, planetary vorticity advection) determine the evolution of potential vorticity.

The upper layer potential vorticity budget over the black box in Fig. 9a can be written as

$$\begin{aligned} \frac{\partial \overline{q_1}}{\partial t} = & \text{TPV1} + \text{TPV2} + \text{TPV3} + \text{TPV4} + \text{RPV1} \\ & + \text{RPV2} + \text{RPV3} + \text{RPV4} + \text{Betae} + \text{Beta} \\ & + \text{LF} + \text{LFe} + \text{Res}, \end{aligned} \quad (4)$$

where the meaning of each term is listed in Table 2. The detailed derivation and formulas of terms are given in the appendix.

The potential vorticity budget equation shows which processes determine the changes of the potential vorticity. TPV1 and RPV1 are the influence by the mean flow changes, representing the mean flow relative vorticity and thickness vorticity advected by mean flow, respectively. And TPV4 and RPV4 are influenced by the eddy activity changes, representing the eddy relative vorticity and eddy thickness vorticity advected by eddy activity. Besides, the TPV2, TPV3, RPV2, and RPV3 show the potential vorticity advected by the eddy–mean flow interaction. Beta and Betae are the planetary vorticity advected by mean flow and eddy activity, respectively. LF and LFe are the lateral dissipation by mean flow and eddy activity, respectively.

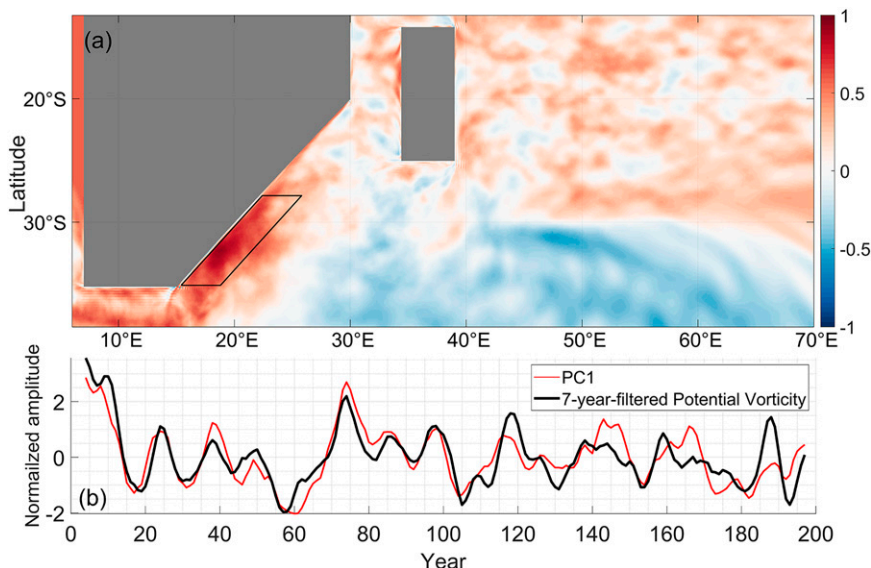


FIG. 9. (a) Correlations between potential vorticity changes and the dipole-mode variability. The potential vorticity is 7-yr low-pass filtered before the correlation. The black box indicates the region used for potential vorticity budget analysis in section 4c. (b) Time series of the low-frequency dipole mode (red line) and potential vorticity averaged over the black box in (a) (black line).

First, we investigate the potential vorticity balance in the mean state by calculating a time mean of Eq. (4) (Fig. 10). We show that the planetary vorticity, thickness vorticity and relative vorticity advection by the mean flow ($\text{Beta} + \text{TPV1} + \text{TRV1}$) tend to increase the potential vorticity in the AC region, which is largely in balance with eddy activity (RPV4). Physically, this means that the shear increases as Coriolis decreases southward to conserve angular momentum, while the eddy activity acts to decrease the horizontal shear by mixing the momentum between the core and flank of the current. The potential vorticity divergence terms due to lateral dissipation and interactions between eddies and the mean flow have little effect on the time-mean potential vorticity balance, suggesting that the AC in our QG simulations is in the regime of nonlinear inertial boundary currents (Pedlosky 1996).

TABLE 2. Meaning of each term in Eq. (4).

Term	Meaning
TPV1	Divergence of TPV by mean flow
TPV2	Divergence of eddy TPV by mean flow
TPV3	Divergence of mean flow TPV by eddy
TPV4	Divergence of TPV by eddy
RPV1	Divergence of RPV by mean flow
RPV2	Divergence of eddy RPV by mean flow
RPV3	Divergence of mean flow RPV by eddy
RPV4	Divergence of RPV by eddy
Beta	Planetary vorticity advection by mean flow
Betae	Planetary vorticity advection by eddy
LF	Lateral dissipation by mean flow
LF _e	Lateral dissipation by eddy
Res	Wind input and errors caused by calculation

Then we examine how each term of the potential vorticity budget differs between different phases of the dipole mode. We calculate a composite of each term of the potential vorticity budget, with the time-mean value subtracted, during the positive phase and negative phase of the dipole mode (Fig. 11). We find that when the potential vorticity is high (low) in the AC region, the RPV4 (i.e., eddy relative vorticity advected by eddy activity) contributes most of the positive (negative) potential vorticity anomaly, while Beta, TPV1, TPV4, and LF tend to partially offset the change of RPV4. The low-frequency potential vorticity variability is closely connected to changes in the eddy-driven RPV4, with a correlation coefficient around 0.7 (Fig. 11c). Thus, we conclude that the low-frequency dipole mode variability is largely driven by changes in the eddy activity: when the eddy activity becomes stronger, the momentum mixing between the core and flank of the AC is enhanced, leading to a decrease in the horizontal shear of the AC.

5. Discussion

a. Long-term trends of the two modes

In the preindustrial control run, the uniform and dipole modes lack linear trends on multicentennial time scales due to the constant climate forcing. And both modes present substantial internal variability on decadal and multidecadal time scales, suggesting the volume transport and the width of AC oscillate on decadal to multidecadal time scales. Unlike the preindustrial control run, the uniform mode in the historical run has an explicit trend over 120 years, suggesting a decline of volume transport in response to anthropogenic forcing. We confirm this by

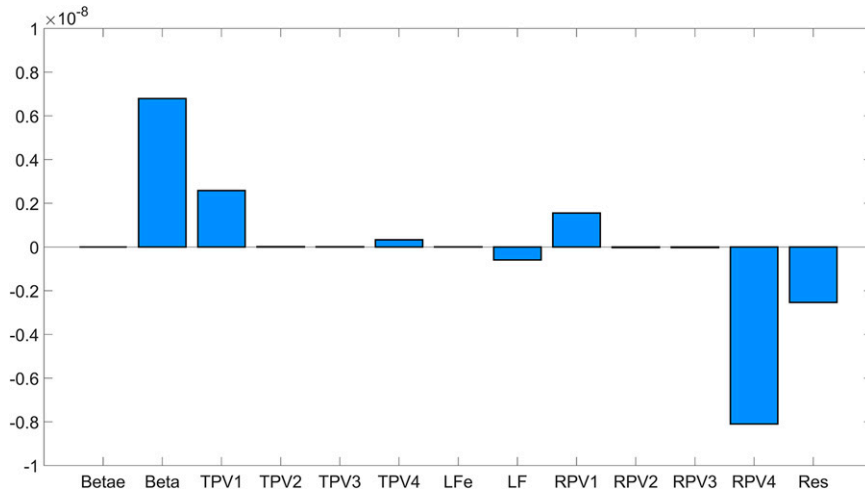


FIG. 10. Time mean of each term in the potential vorticity budget [Eq. (4)].

calculating the trends of the uniform mode in each 120-yr segment in the preindustrial control run and showing the probability density function (PDF) of these trends. The trend of uniform mode in the historical run lies on the tail of the PDF of the uniform mode in the preindustrial control (Fig. S19), suggesting that this 120-yr trend is more likely forced by the anthropogenic forcing. A 24-yr observation-based record also exhibits a declining trend in the AC volume transport (Beal and Elipot 2016), which might be caused by a combination of anthropogenic forcing and internal variability as the volume transport is also significantly affected by the internal variability in decadal time scale (Fig. 4).

The dipole mode in the historical run presents no significant trend on centennial time scales and its spatial pattern appears

to be comparable with observations which suggest a broadening AC since the 1990s (Beal and Elipot 2016). The spatial pattern of the broadening in Beal and Elipot (2016) is similar to our dipole mode in transition from a negative phase to a positive phase (i.e., a shift from a faster core to a faster flank) in two decades in the CESM. In the historical run, the lack of long-term trend in the dipole mode suggests that the transition between different phases is not likely a signal of anthropogenic forcing. Thus, we argue that the broadening of AC in the 24-yr observation might be caused by the internal variability. To confirm this, we define the AC width as the distance between the western boundary and the position where the vertical integration of velocity reaches $100 \text{ m}^2 \text{ s}^{-1}$ and calculate its changes in each 24-yr segment in the preindustrial

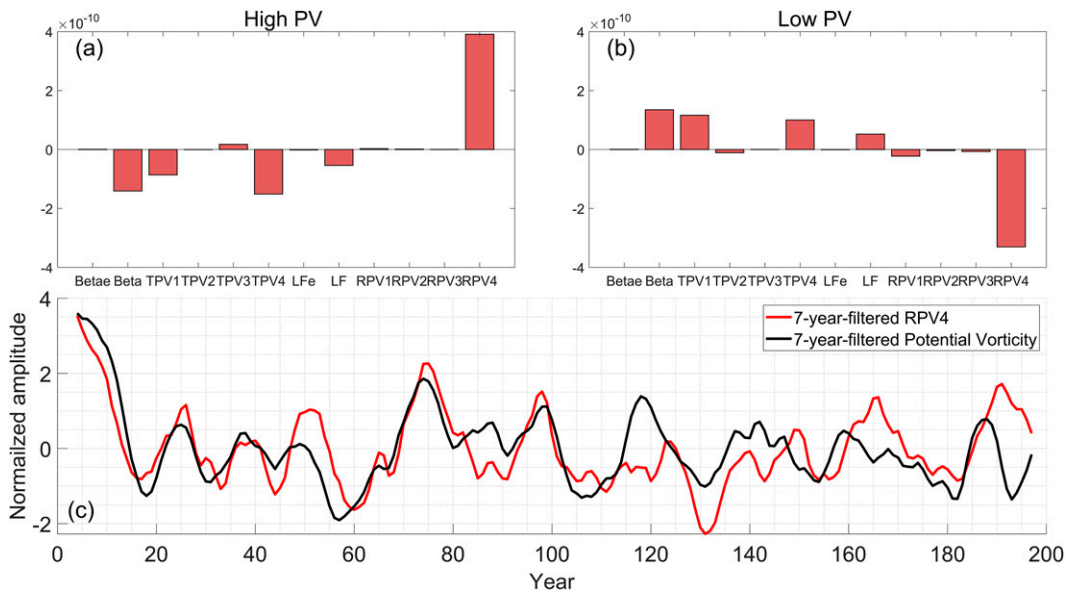


FIG. 11. (a) Difference of each term in Eq. (4) between the (a) the negative phase and (b) the positive phase of the dipole mode with the mean state. (c) Low-pass-filtered potential vorticity (black) and low-pass filtered RVP4 (red).

control run. Then we compare their PDF with the observation (Fig. S20). With the same definition, the observed broadening of the AC by around 25 km between 1993 and 2015 is well within the internal variability in CESM, suggesting that this 24-yr change in AC width is more likely caused by internal variability. Nonetheless, a recent study suggests that the ocean eddy activity will intensify in the twenty-first century in the Agulhas Current region (Beech et al. 2022). The stronger eddy activity may cause the AC to become broader in the future enhanced warming climate (e.g., Beal and Elipot 2016).

b. Sensitive experiments of the QG model

We carry out a series of QG model experiments to examine the sensitivity to different parameters and model configurations. The presence of the dipole mode appears to be rather insensitive to changes in the lateral dissipation rate over the range of $120\text{--}200\text{ m}^2\text{ s}^{-1}$ and the dipole mode accounts for at least 60% of the total variance regardless of the lateral dissipation rate. We discuss the role of nonlinearity in modulating the low-frequency variability of AC by removing the nonlinear terms in Eq. (1). In this run (Fig. S21), the width of AC is 50 km and the core speed of AC is near 5 m s^{-1} . The first two modes could explain 99.9% of the total variance. During the spinup, the EOF1 and EOF2 resemble the dipole mode and uniform mode in nonlinear run, and the principal components of these two modes exhibit periodic variability, whereas the amplitudes of the two modes decrease dramatically as time. When the linearized QG model integrates beyond 70 years, the AC does not change anymore. This result highlights the role of nonlinearity in the formation of low-frequency variability in ocean intrinsic processes.

c. Implications and caveats

The low-frequency variability of AC might play a significant role in modulating the climate. The dipole mode suggests the width of AC shows substantial decadal variability. The AC width changes could affect the thermohaline property of AC (Gunn et al. 2020; McMonigal et al. 2020) and thus the salt transport by the Agulhas leakage into the Atlantic, potentially affecting the AMOC variability (Weijer et al. 2002; Biastoch et al. 2008b). The uniform mode may also be relevant to the interbasin exchanges. When the volume transport of AC is low, associated with the long-term trend of the uniform mode, the Agulhas Current detaches farther downstream from the African continental slope and leads to more Agulhas leakage (van Sebille et al. 2009). Thus, the trend of the uniform mode would induce more Agulhas leakage, leading to more salt transport into the Atlantic basin, which could offset the slowdown of the AMOC in a warming climate (Beal et al. 2011; Weijer et al. 2002).

Our results highlight the role of internal dynamics in controlling the Agulhas Current on decadal to multidecadal time scales. Thus, we should be cautious in interpreting the anthropogenic signals in the circulation system. Our results also highlight the role of eddy activity in modulating the western boundary currents, which suggests potential caveats in previous studies on the western boundary currents that rely on coarse-resolution

models (e.g., Peng et al. 2022). In the high-resolution CESM simulation, the western boundary currents in the other areas also exhibit substantial variability on a range of time scales. In response to a warming climate, the volume transports of these western boundary currents also show significant changes, but not uniformly. Specifically, the Agulhas Current and Gulf Stream weaken, while the Kuroshio and Brazil Current become stronger, consistent with previous climate model simulations (Sen Gupta et al. 2021). In the other ocean basins, the western boundary currents also present changes in their path and structure, reminiscent of the dipole mode in this study (e.g., the “large meander” of Kuroshio; Qiu and Chen 2021).

Moreover, although we argue the uniform mode is a response to the external low-frequency wind variability in the Indian Ocean, other processes (e.g., eddy activity, basin mode, air–sea interaction) might also contribute to it (Y. Zhang et al. 2020; Cessi and Louazel 2001; Yang et al. 2017a; Ma et al. 2016). In the QG model experiment, the uniform mode accounts for 18% of the total variance despite a lack of wind variability (Figs. 7b,d). Besides, the two leading modes in both the preindustrial control and historical CESM simulations show substantial decadal and multidecadal variability. But the spectrums of the two modes are not exactly the same between the preindustrial control and historical simulation, which might be caused by the evolution of natural variability (e.g., ENSO, SAM, etc.) (Elipot and Beal 2018; Cai et al. 2015; Fogt and Marshall 2020; Cai et al. 2005; Wang et al. 2017). Finally, although the high-resolution CESM show significant improvements as compared to the coarse-resolution climate models (Chang et al. 2020), the topography is still quite blocky compared to the real ocean. Thus, more observations are still needed to monitor the multi-time-scale AC variability (Gunn et al. 2020; McMonigal et al. 2020).

6. Summary

Using a hierarchy of high-resolution climate/ocean models, the low-frequency variability of the AC and its physical mechanisms are investigated in this study. Two predominant modes, a uniform mode and a dipole mode, are identified, which could explain much of the low-frequency AC variance. The uniform mode, which is associated with the volume transport changes of the AC, is mainly driven by the low-frequency variability of the wind field in the Indian Ocean. The dipole mode, which is associated with the width changes of the AC, is attributed to the low-frequency variability of eddy activity.

Comparing results from the preindustrial control experiment with a historical experiment, which include historical anthropogenic forcing, we find a predominant decline of AC volume transport from 1850 to 2005. The weakening of the AC could lead to a strengthening of the Agulhas Leakage (van Sebille et al. 2009) and partially compensate for the AMOC weakening in a warming climate (e.g., Bonan et al. 2022).

We use a two-layer QG model to show the dynamics involved in the dipole mode. Through a potential vorticity budget, we demonstrate that eddy activity is essential in driving the low-frequency dipole mode. Although our results are robust across a hierarchy of high-resolution climate/ocean models and limited

observations appear to exhibit similar changes, more state-of-the-art climate models and a longer observational record are needed to verify our results, particularly the response of the AC to the continued warming due to greenhouse gas forcing.

Acknowledgments. This research is funded by National Natural Science Foundation of China (42225601, 42076009, 41822601, and 41806008). Z. C. is partially supported by Taishan Scholar Funds (tsqn201812022) and Fundamental Research Funds for the Central Universities (202072001). We thank Yan Wang for a helpful discussion. We are grateful for the constructive comments from two anonymous reviewers that helped improve the manuscript.

Data availability statement. The high-resolution CESM simulations used in this work are available from both iHESP data portal (<https://ihesp.github.io/archive/>) and QNLM data portal (<http://ihesp.qnlnm.ac>). And the CMIP6 HighResMIP simulations are available in the ESGF (<https://esgf-node.llnl.gov/search/cmip6/>). The source code for the QG model can be accessed from <https://github.com/ocai-rz/RAY>.

APPENDIX

Potential Vorticity Budget

The potential vorticity budget equation associated with mean flow and eddy activity is derived. By decomposing the total streamfunction into the mean flow (frequency < 18 months) and eddy activity (frequency > 18 months) as $\psi_i = \Psi_i + \varphi_i$ and then substituting it into Eq. (1a), we could obtain the potential vorticity budget equation in the upper layer:

$$\begin{aligned} \frac{\partial q_1}{\partial t} = & -J(\Psi_1, \nabla^2 \Psi_1) - J(\Psi_1, \nabla^2 \varphi_1) - J(\varphi_1, \nabla^2 \Psi_1) \\ & - J(\varphi_1, \nabla^2 \varphi_1) - \frac{f_0^2}{g'H_1} J(\Psi_1, \Psi_2) - \frac{f_0^2}{g'h_1} J(\Psi_1, \varphi_2) \\ & - \frac{f_0^2}{g'h_1} J(\varphi_1, \Psi_2) - \frac{f_0^2}{g'h_1} J(\varphi_1, \varphi_2) - \beta \frac{\partial \Psi_1}{\partial x} - \beta \frac{\partial \varphi_1}{\partial x} \\ & + A_H \nabla^4 \Psi_1 + A_H \nabla^4 \varphi_1 + \frac{f_0}{H_1} W. \end{aligned} \quad (\text{A1})$$

Taking the 7-yr moving average filter of Eq. (A1), we could obtain

$$\begin{aligned} \widetilde{\frac{\partial q_1}{\partial t}} = & -J(\widetilde{\Psi_1}, \nabla^2 \widetilde{\Psi_1}) - J(\widetilde{\Psi_1}, \nabla^2 \widetilde{\varphi_1}) - J(\widetilde{\varphi_1}, \nabla^2 \widetilde{\Psi_1}) \\ & - J(\widetilde{\varphi_1}, \nabla^2 \widetilde{\varphi_1}) - \frac{f_0^2}{g'H_1} J(\widetilde{\Psi_1}, \widetilde{\Psi_2}) - \frac{f_0^2}{g'h_1} J(\widetilde{\Psi_1}, \widetilde{\varphi_2}) \\ & - \frac{f_0^2}{g'h_1} J(\widetilde{\varphi_1}, \widetilde{\Psi_2}) - \frac{f_0^2}{g'h_1} J(\widetilde{\varphi_1}, \widetilde{\varphi_2}) - \beta \frac{\partial \widetilde{\Psi_1}}{\partial x} - \beta \frac{\partial \widetilde{\varphi_1}}{\partial x} \\ & + \widetilde{A_H \nabla^4 \Psi_1} + \widetilde{A_H \nabla^4 \varphi_1} + \frac{f_0}{H_1} W. \end{aligned} \quad (\text{A2})$$

Here, a tilde ($\widetilde{\quad}$) indicates a 7-yr low-pass filter.

REFERENCES

- Beal, L. M., and S. Elipot, 2016: Broadening not strengthening of the Agulhas Current since the early 1990s. *Nature*, **540**, 570–573, <https://doi.org/10.1038/nature19853>.
- , W. P. De Ruijter, A. Biastoch, R. Zahn, and SCOR/WCRP/IAPSO Working Group, 2011: On the role of the Agulhas system in ocean circulation and climate. *Nature*, **472**, 429–436, <https://doi.org/10.1038/nature09983>.
- , S. Elipot, A. Houk, and G. M. Leber, 2015: Capturing the transport variability of a western boundary jet: Results from the Agulhas Current Time-Series Experiment (ACT). *J. Phys. Oceanogr.*, **45**, 1302–1324, <https://doi.org/10.1175/JPO-D-14-0119.1>.
- Beech, N., T. Rackow, T. Semmler, S. Danilov, Q. Wang, and T. Jung, 2022: Long-term evolution of ocean eddy activity in a warming world. *Nat. Climate Change*, **12**, 910–917, <https://doi.org/10.1038/s41558-022-01478-3>.
- Berloff, P., and S. P. Meacham, 1998: The dynamics of a simple baroclinic model of the wind-driven circulation. *J. Phys. Oceanogr.*, **28**, 361–388, [https://doi.org/10.1175/1520-0485\(1998\)028<0361:TDOASB>2.0.CO;2](https://doi.org/10.1175/1520-0485(1998)028<0361:TDOASB>2.0.CO;2).
- , and J. C. McWilliams, 1999a: Quasigeostrophic dynamics of the western boundary current. *J. Phys. Oceanogr.*, **29**, 2607–2634, [https://doi.org/10.1175/1520-0485\(1999\)029<2607:QDOTWB>2.0.CO;2](https://doi.org/10.1175/1520-0485(1999)029<2607:QDOTWB>2.0.CO;2).
- , and —, 1999b: Large-scale, low-frequency variability in wind-driven ocean gyres. *J. Phys. Oceanogr.*, **29**, 1925–1949, [https://doi.org/10.1175/1520-0485\(1999\)029<1925:LSLFVI>2.0.CO;2](https://doi.org/10.1175/1520-0485(1999)029<1925:LSLFVI>2.0.CO;2).
- , A. M. C. Hogg, and W. Dewar, 2007: The turbulent oscillator: A mechanism of low-frequency variability of the wind-driven ocean gyres. *J. Phys. Oceanogr.*, **37**, 2363–2386, <https://doi.org/10.1175/JPO3118.1>.
- Biastoch, A., J. R. E. Lutjeharms, C. W. Böning, and M. Scheinert, 2008a: Mesoscale perturbations control inter-ocean exchange south of Africa. *Geophys. Res. Lett.*, **35**, L20602, <https://doi.org/10.1029/2008GL035132>.
- , C. W. Böning, and J. Lutjeharms, 2008b: Agulhas leakage dynamics affects decadal variability in Atlantic overturning circulation. *Nature*, **456**, 489–492, <https://doi.org/10.1038/nature07426>.
- , C. W. Böning, F. U. Schwarzkopf, and J. R. Lutjeharms, 2009: Increase in Agulhas leakage due to poleward shift of Southern Hemisphere westerlies. *Nature*, **462**, 495–498, <https://doi.org/10.1038/nature08519>.
- Bonan, D. B., A. F. Thompson, E. R. Newsom, S. Sun, and M. Rugestein, 2022: Transient and equilibrium responses of the Atlantic overturning circulation to warming in coupled climate models: The role of temperature and salinity. *J. Climate*, **35**, 5173–5193, <https://doi.org/10.1175/JCLI-D-21-0912.1>.
- Cai, W., 2006: Antarctic ozone depletion causes an intensification of the Southern Ocean super-gyre circulation. *Geophys. Res. Lett.*, **33**, L03712, <https://doi.org/10.1029/2005GL024911>.
- , G. Shi, T. Cowan, D. Bi, and J. Ribbe, 2005: The response of the Southern Annular Mode, the East Australian Current, and the southern mid-latitude ocean circulation to global warming. *Geophys. Res. Lett.*, **32**, L23706, <https://doi.org/10.1029/2005GL024701>.
- , and Coauthors, 2015: ENSO and greenhouse warming. *Nat. Climate Change*, **5**, 849–859, <https://doi.org/10.1038/nclimate2743>.
- Cessi, P., and G. R. Ierley, 1995: Symmetry-breaking multiple equilibria in quasigeostrophic, wind-driven flows. *J. Phys. Oceanogr.*,

- 25, 1196–1205, [https://doi.org/10.1175/1520-0485\(1995\)025<1196:SBMEIQ>2.0.CO;2](https://doi.org/10.1175/1520-0485(1995)025<1196:SBMEIQ>2.0.CO;2).
- , and S. Louazel, 2001: Decadal oceanic response to stochastic wind forcing. *J. Phys. Oceanogr.*, **31**, 3020–3029, [https://doi.org/10.1175/1520-0485\(2001\)031<3020:DORTSW>2.0.CO;2](https://doi.org/10.1175/1520-0485(2001)031<3020:DORTSW>2.0.CO;2).
- Chang, K., M. Ghil, K. Ide, and C. Lai, 2001: Transition to aperiodic variability in a wind-driven double-gyre circulation model. *J. Phys. Oceanogr.*, **31**, 1260–1286, [https://doi.org/10.1175/1520-0485\(2001\)031<1260:TTAVIA>2.0.CO;2](https://doi.org/10.1175/1520-0485(2001)031<1260:TTAVIA>2.0.CO;2).
- Chang, P., and Coauthors, 2020: An unprecedented set of high-resolution Earth system simulations for understanding multi-scale interactions in climate variability and change. *J. Adv. Model. Earth Syst.*, **12**, e2020MS002298, <https://doi.org/10.1029/2020MS002298>.
- Chassignet, E. P., and X. Xu, 2021: On the importance of high-resolution in large-scale ocean models. *Adv. Atmos. Sci.*, **38**, 1621–1634, <https://doi.org/10.1007/s00376-021-0385-7>.
- Dewar, W., 2003: Nonlinear midlatitude ocean adjustment. *J. Phys. Oceanogr.*, **33**, 1057–1082, [https://doi.org/10.1175/1520-0485\(2003\)033<1057:NMOA>2.0.CO;2](https://doi.org/10.1175/1520-0485(2003)033<1057:NMOA>2.0.CO;2).
- Elipot, S., and L. M. Beal, 2015: Characteristics, energetics, and origins of Agulhas Current meanders and their limited influence on ring shedding. *J. Phys. Oceanogr.*, **45**, 2294–2314, <https://doi.org/10.1175/JPO-D-14-0254.1>.
- , and —, 2018: Observed Agulhas Current sensitivity to interannual and long-term trend atmospheric forcings. *J. Climate*, **31**, 3077–3098, <https://doi.org/10.1175/JCLI-D-17-0597.1>.
- Fogt, R. L., and G. J. Marshall, 2020: The Southern Annular Mode: Variability, trends, and climate impacts across the Southern Hemisphere. *Wiley Interdiscip. Rev.: Climate Change*, **11**, e652, <https://doi.org/10.1002/wcc.652>.
- Gunn, K. L., L. M. Beal, S. Elipot, K. McMonigal, and A. Houk, 2020: Mixing of subtropical, central, and intermediate waters driven by shifting and pulsing of the Agulhas Current. *J. Phys. Oceanogr.*, **50**, 3545–3560, <https://doi.org/10.1175/JPO-D-20-0093.1>.
- , K. McMonigal, L. M. Beal, and S. Elipot, 2022: Decadal and intra-annual variability of the Indian Ocean freshwater budget. *J. Phys. Oceanogr.*, **52**, 2361–2376, <https://doi.org/10.1175/JPO-D-22-0057.1>.
- Haarsma, R. J., and Coauthors, 2016: High Resolution Model Inter-comparison Project (HighResMIP v1.0) for CMIP6. *Geosci. Model Dev.*, **9**, 4185–4208, <https://doi.org/10.5194/gmd-9-4185-2016>.
- Hallberg, R., 2013: Using a resolution function to regulate parameterizations of oceanic mesoscale eddy effects. *Ocean Modell.*, **72**, 92–103, <https://doi.org/10.1016/j.ocemod.2013.08.007>.
- Krug, M., and P. Penven, 2011: New perspectives on Natal Pulses from satellite observations. *J. Geophys. Res.*, **116**, C07013, <https://doi.org/10.1029/2010JC006866>.
- Ma, J., M. Feng, J. Lan, and D. Hu, 2020: Projected future changes of meridional heat transport and heat balance of the Indian Ocean. *Geophys. Res. Lett.*, **47**, e2019GL086803, <https://doi.org/10.1029/2019GL086803>.
- Ma, X., and Coauthors, 2016: Western boundary currents regulated by interaction between ocean eddies and the atmosphere. *Nature*, **535**, 533–537, <https://doi.org/10.1038/nature18640>.
- McMonigal, K., L. M. Beal, S. Elipot, K. L. Gunn, J. Hermes, T. Morris, and A. Houk, 2020: The impact of meanders, deepening and broadening, and seasonality on Agulhas Current temperature variability. *J. Phys. Oceanogr.*, **50**, 3529–3544, <https://doi.org/10.1175/JPO-D-20-0018.1>.
- , K. L. Gunn, L. M. Beal, S. Elipot, and J. K. Willis, 2022: Reduction in meridional heat export contributes to recent Indian Ocean warming. *J. Phys. Oceanogr.*, **52**, 329–345, <https://doi.org/10.1175/JPO-D-21-0085.1>.
- Mu, L., L. Zhong, L. Hua, and J. Song, 2011: Low-frequency variability of a semi-closed sea induced by the circulation in an adjacent ocean in a wind-driven, quasi-geostrophic, eddy-resolving simulation. *Ocean Dyn.*, **61**, 1459–1473, <https://doi.org/10.1007/s10236-011-0443-2>.
- Pedlosky, J., 1987: *Geophysical Fluid Dynamics*. 2nd ed. Springer, 710 pp.
- , 1996: *Ocean Circulation Theory*. Springer, 453 pp.
- Peng, Q., S.-P. Xie, D. Wang, R. X. Huang, G. Chen, Y. Shu, J.-R. Shi, and W. Liu, 2022: Surface warming-induced global acceleration of upper ocean currents. *Sci. Adv.*, **8**, eabj8394, <https://doi.org/10.1126/sciadv.abj8394>.
- Qiu, B., and S. Chen, 2021: Revisit of the occurrence of the Kuroshio large meander south of Japan. *J. Phys. Oceanogr.*, **51**, 3679–3694, <https://doi.org/10.1175/JPO-D-21-0167.1>.
- Roberts, M. J., and Coauthors, 2020: Sensitivity of the Atlantic meridional overturning circulation to model resolution in CMIP6 HighResMIP simulations and implications for future changes. *J. Adv. Model. Earth Syst.*, **12**, e2019MS002014, <https://doi.org/10.1029/2019MS002014>.
- Rouault, M., P. Penven, and B. Pohl, 2009: Warming in the Agulhas Current system since the 1980's. *Geophys. Res. Lett.*, **36**, L12602, <https://doi.org/10.1029/2009GL037987>.
- Rühs, S., J. V. Durgadoo, E. Behrens, and A. Biastoch, 2013: Advective timescales and pathways of Agulhas leakage. *Geophys. Res. Lett.*, **40**, 3997–4000, <https://doi.org/10.1002/grl.50782>.
- Sen Gupta, A., A. Stellema, G. M. Pontes, A. S. Taschetto, A. Vergés, and V. Rossi, 2021: Future changes to the upper ocean western boundary currents across two generations of climate models. *Sci. Rep.*, **11**, 9538, <https://doi.org/10.1038/s41598-021-88934-w>.
- Smith, R. D., M. E. Maltrud, F. O. Bryan, and M. W. Hecht, 2000: Numerical simulation of the North Atlantic Ocean at 1/10°. *J. Phys. Oceanogr.*, **30**, 1532–1561, [https://doi.org/10.1175/1520-0485\(2000\)030<1532:NSOTNA>2.0.CO;2](https://doi.org/10.1175/1520-0485(2000)030<1532:NSOTNA>2.0.CO;2).
- Stellema, A., A. Sen Gupta, and A. S. Taschetto, 2019: Projected slow down of South Indian Ocean circulation. *Sci. Rep.*, **9**, 17705, <https://doi.org/10.1038/s41598-019-54092-3>.
- Sun, S., L. Wu, and B. Qiu, 2013: Response of the inertial recirculation to intensified stratification in a two-layer quasigeostrophic ocean circulation model. *J. Phys. Oceanogr.*, **43**, 1254–1269, <https://doi.org/10.1175/JPO-D-12-0111.1>.
- Sverdrup, H. U., 1947: Wind-driven currents in a baroclinic ocean; with application to the equatorial currents of the eastern Pacific. *Proc. Natl. Acad. Sci. USA*, **33**, 318–326, <https://doi.org/10.1073/pnas.33.11.318>.
- Talley, L. D., 2013: Closure of the global overturning circulation through the Indian, Pacific, and Southern Oceans: Schematics and transports. *Oceanography*, **26**, 80–97, <https://doi.org/10.5670/oceanog.2013.07>.
- Tsugawa, M., and H. Hasumi, 2010: Generation and growth mechanism of the Natal Pulse. *J. Phys. Oceanogr.*, **40**, 1597–1612, <https://doi.org/10.1175/2010JPO4347.1>.
- van Sebille, E., A. Biastoch, P. J. van Leeuwen, and W. P. M. de Ruijter, 2009: A weaker Agulhas Current leads to more Agulhas leakage. *Geophys. Res. Lett.*, **36**, L03601, <https://doi.org/10.1029/2008GL036614>.
- Wang, G., W. Cai, B. Gan, L. Wu, A. Santoso, X. Lin, Z. Chen, and M. J. McPhaden, 2017: Continued increase of extreme El Niño frequency long after 1.5°C warming stabilization. *Nat. Climate Change*, **7**, 568–572, <https://doi.org/10.1038/nclimate3351>.

- Wang, Y., F. J. Beron-Vera, and M. J. Olascoaga, 2016: The life cycle of a coherent Lagrangian Agulhas ring. *J. Geophys. Res. Oceans*, **121**, 3944–3954, <https://doi.org/10.1002/2015JC011620>.
- Weijer, W., W. P. De Ruijter, and H. A. Dijkstra, 2001: Stability of the Atlantic overturning circulation: Competition between Bering Strait freshwater flux and Agulhas heat and salt sources. *J. Phys. Oceanogr.*, **31**, 2385–2402, [https://doi.org/10.1175/1520-0485\(2001\)031<2385:SOTAOC>2.0.CO;2](https://doi.org/10.1175/1520-0485(2001)031<2385:SOTAOC>2.0.CO;2).
- , —, A. Sterl, and S. S. Drijfhout, 2002: Response of the Atlantic overturning circulation to South Atlantic sources of buoyancy. *Global Planet. Change*, **34**, 293–311, [https://doi.org/10.1016/S0921-8181\(02\)00121-2](https://doi.org/10.1016/S0921-8181(02)00121-2).
- Yamagami, Y., T. Tozuka, and B. Qiu, 2019: Interannual variability of the Natal Pulse. *J. Geophys. Res. Oceans*, **124**, 9258–9276, <https://doi.org/10.1029/2019JC0015525>.
- Yang, H., L. Wu, S. Sun, and Z. Chen, 2015: Low-frequency variability of monsoon-driven circulation with application to the South China Sea. *J. Phys. Oceanogr.*, **45**, 1632–1650, <https://doi.org/10.1175/JPO-D-14-0212.1>.
- , G. Lohmann, W. Wei, M. Dima, M. Ionita, and J. Liu, 2016: Intensification and poleward shift of subtropical western boundary currents in a warming climate. *J. Geophys. Res. Oceans*, **121**, 4928–4945, <https://doi.org/10.1002/2015JC011513>.
- , L. Wu, S. Sun, and Z. Chen, 2017a: Selective response of the South China Sea circulation to summer monsoon. *J. Phys. Oceanogr.*, **47**, 1555–1568, <https://doi.org/10.1175/JPO-D-16-0288.1>.
- , —, —, and —, 2017b: Role of the South China Sea in regulating the North Pacific double-gyre system. *J. Phys. Oceanogr.*, **47**, 1617–1635, <https://doi.org/10.1175/JPO-D-16-0272.1>.
- , and Coauthors, 2020: Poleward shift of the major ocean gyres detected in a warming climate. *Geophys. Res. Lett.*, **47**, e2019GL085868, <https://doi.org/10.1029/2019GL085868>.
- Zhang, L., L. Wu, X. Lin, and D. Wu, 2010: Modes and mechanisms of sea surface temperature low-frequency variations over the coastal China seas. *J. Geophys. Res.*, **115**, C08031, <https://doi.org/10.1029/2009JC006025>.
- Zhang, S., and Coauthors, 2020: Optimizing high-resolution Community Earth System Model on a heterogeneous many-core supercomputing platform. *Geosci. Model Dev.*, **13**, 4809–4829, <https://doi.org/10.5194/gmd-13-4809-2020>.
- Zhang, Y., Z. Zhang, D. Chen, B. Qiu, and W. Wang, 2020: Strengthening of the Kuroshio Current by intensifying tropical cyclones. *Science*, **368**, 988–993, <https://doi.org/10.1126/science.aax5758>.